RESEARCH ARTICLE

Steady Cu+ species *via* magnesium and boron co-modification for enhanced CO_2 electroreduction to C_{2+} products: an *in situ* Raman spectroscopic study†

Hua Yang,[a] Xuefan Mu,[a] Jiexin Guan,[a] Bo Ouyang,[b] Huaming Li [ID][a] and Yilin Deng [ID] *[a]

The electrochemical carbon dioxide reduction reaction (CO_2RR) to produce high-value multi-carbon (C_{2+}) compounds holds significant practical importance in realizing carbon neutrality. Copper-based electrocatalysts are promising for CO_2-to-C_{2+} conversion. However, the labile Cu valence at high current densities impedes C_{2+} product generation. Here, we present an electrocatalyst derived from CuO, featuring a heterostructure of $Cu/Cu_2O/CuO/Mg(OH)_2$ *via* the co-addition of Mg and B during the preparation (referred to as $Cu_5(B_{0.02\ M})Mg_1$). The $Cu_5(B_{0.02\ M})Mg_1$ shows an impressive C_{2+} yield, with a Faraday efficiency ($FE_{C_{2+}}$) of 79.59% at −1.57 V *vs.* RHE (reversible hydrogen electrode). Additionally, the partial current density of C_{2+} on the $Cu_5(B_{0.02\ M})Mg_1$ catalyst is −317.03 mA cm^{-2}, 2.7 and 3.5 times higher than those catalysts lacking B (Cu_5Mg_1 catalyst) or Mg ($Cu(B_{0.02\ M})$ catalyst), respectively. Over a wide potential range of 600 mV between −1.17 and −1.77 V *vs.* RHE, the overall $FE_{C_{2+}}$ surpasses 60% on the $Cu_5(B_{0.02\ M})Mg_1$ catalyst. X-ray diffraction (XRD), X-ray photoelectron spectroscopy (XPS) and high-resolution transmission electron microscopy (HRTEM) characterization studies indicate the $NaBH_4$ reactant could promote the formation of crystalline $Mg(OH)_2$ in the catalyst structure, which is found to better stabilize Cu+ at negative potentials compared to the amorphous phase. Further *in situ* Raman spectroscopy reveals that at increasingly negative potentials, the higher copper species (Cu^{2+}) is inevitably reduced to the lower copper species (Cu^0/Cu^+). However, the synergy of Mg and B prolongs the presence of Cu+ on the catalyst surface across a broad potential range, and *CO and $*CO_2^-$ could still be recorded at quite negative reduction potentials. This suggests enhanced binding strength of *CO intermediates on the catalyst surface, promoting the C−C coupling process.

1. Introduction

The electrocatalytic carbon dioxide reduction reaction (CO_2RR) represents a pathway for producing high-value-added chemicals and fuels, offering a means to reduce global carbon dioxide (CO_2) emissions and alleviate the shortage of non-renewable carbon resources.[1–3] The CO_2RR yields primarily hydrocarbons and oxygen-containing compounds. Among them, multi-carbon (C_{2+}) products such as ethylene (C_2H_4) and ethanol (C_2H_5OH) have broader industrial applications and higher energy densities compared with C_1 products like

carbon monoxide (CO) and methane (CH_4), thus commanding a higher economic value per unit mass.[4–6] However, challenges persist due to the requirement of a significant amount of energy to break the C=O bond with the high dissociation energy of CO_2 (about 750 kJ mol^{-1}). Furthermore, the multi-step proton-coupling process contributes to the poor selectivity and yield of target products during the CO_2RR.[7–9] Addressing these issues requires the exploration and design of electrocatalysts with enhanced efficiency to facilitate CO_2 conversion while minimizing product distribution variability during the CO_2RR process.

To date, copper-based materials, which have been found crucial for C−C coupling, remain the major electrocatalysts for efficiently converting CO_2 to long-chain hydrocarbons and multi-carbon oxygenates.[10–12] Previous studies suggest that Cu+ species on Cu-based materials could enhance the selectivity of C_{2+} products.[13,14] However, under high-current electrolysis, particularly at the negative potentials required for C_{2+}

[a]Institute for Energy Research, Jiangsu University, Zhenjiang 212013, China. E-mail: yldeng@ujs.edu.cn
[b]Department of Applied Physics and Institution of Energy and Microstructure, Nanjing University of Science and Technology, Nanjing 210094, China

product formation, the catalyst structure becomes unstable, and Cu^+ is readily reduced to Cu^0 during the CO_2RR. Consequently, prolonging the lifetime of Cu^+ at reduction potentials is a current research focus. To preserve Cu^+ during the CO_2RR so as to enhance C_{2+} formation, essential steps involve generating Cu^+ sites and optimizing intermediate adsorption. Researchers have developed several strategies for this purpose, including doping modification,[15,16] addition of different metallic elements,[17,18] heterogeneous interface engineering,[19,20] oxidation state regulation,[21–23] defect control,[21,24–26] *etc.* Until now, nonmetallic elements such as B, C, F, and S have been reported to effectively regulate the electronic structure and stabilize Cu^+ in Cu lattices, facilitating the reduction of CO_2 to C_{2+} products at large current densities.[27–29] For example, Yao *et al.* devised a B-Cu_2O catalyst which showed high selectivity for ethanol product. Their oxygen programmed desorption and density functional theory (DFT) calculations confirmed that B prevented lattice oxygen from separating out from Cu_2O, thereby stabilizing Cu^+ species on the B-Cu_2O surface. This was believed to strengthen Cu–O bonds, significantly enhancing C–C coupling and facilitating the formation of C_{2+} products.[30] Alkaline-earth metals such as Mg, Ba and Ca were found to not only maintain Cu^+ on catalyst surfaces, but also enhance the adsorption of intermediates at active centers, thereby influencing the reaction kinetics of the CO_2RR process.[31] For instance, Peng *et al.* synthesized a nano-Cu_2Mg intermetallic catalyst predominantly oriented along the (111) crystal face on a carbon black substrate (denoted as $Cu_2Mg(111)$). *In situ* Raman spectroscopy and DFT calculations confirmed that the $Cu_3^{\delta-}$–$Mg^{\delta+}$ active sites in $Cu_2Mg(111)$ enhanced the coverage of *CO on the catalyst surface, lowered the energy barrier for *CO–CO coupling, and stabilized the *CHCHOH intermediates to promote ethanol production.[32] In addition, Xie *et al.* engineered a Mg-modified Cu_xO nanoparticle catalyst targeting the C_2H_4 product. *In situ* XRD, *in situ* Raman spectroscopy and DFT calculations demonstrated that the amorphous $Mg(OH)_2$ species stabilized Cu^+ species, promoting the presence of vital high *CO intermediates for C_{2+} products.[33] However, challenges still exist regarding these Cu-based materials specially designed for C_{2+} products. Under current modification measures, Cu^+ has a relatively short lifetime and could only exist within a narrow potential window, significantly limiting its effectiveness during the CO_2RR. Furthermore, there is a lack of literature on the combined effects of alkaline-earth metals and non-metals on copper catalysts. Additionally, the influence of the crystalline or amorphous state of alkaline-earth metal oxides on the stability of Cu^+ has not been thoroughly studied.

Based on the above considerations, we have designed a B-Cu/Cu_2O/CuO/$Mg(OH)_2$ catalyst through a simple two-step protocol involving calcination and wet chemical reduction, aiming to enhance C_{2+} products at high current densities across wide potential ranges. The target catalyst is referred to as $Cu_5(B_{0.02 \text{ M}})Mg_1$, named according to the content of the elements during its preparation. X-ray diffraction (XRD), high-resolution transmission electron microscopy (HRTEM) and *ex*

situ X-ray photoelectron spectroscopy (XPS) reveal that the addition of $NaBH_4$ during catalyst synthesis could promote the formation of crystalline $Mg(OH)_2$ in the catalyst structure, which we suggest would better stabilize Cu^+ compared to the amorphous $Mg(OH)_2$ phase. Further *in situ* Raman investigation confirms that Cu^+ on the $Cu_5(B_{0.02 \text{ M}})Mg_1$ catalyst could persist across a much broader potential window compared to those catalysts lacking crystalline $Mg(OH)_2$ or B. Additionally, the *CO intermediate, a significant precursor of C_{2+} products, is recorded on the $Cu_5(B_{0.02 \text{ M}})Mg_1$ surface even at rather negative potentials during the CO_2RR. Benefiting from the stabilized Cu^+, $Cu_5(B_{0.02 \text{ M}})Mg_1$ shows high selectivity towards C_{2+} within −1.17 to −1.77 V *vs.* RHE (unless specified, all potentials in this work are referenced against RHE). Overall, our work reveals the significance of morphologies of $Mg(OH)_2$ in Cu^+ stabilization and provides a comprehensive understanding of the role of Cu^+ in the efficient CO_2RR towards C_{2+} products.

2. Results and discussion

2.1 Morphological and structural characterization of the catalysts

The typical fabrication process of $Cu_5(B_{0.02 \text{ M}})Mg_1$ is depicted in Fig. 1, with detailed synthesis described in the ESI.† The XRD pattern indicates diffraction peaks of Cu, Cu_2O, CuO and $Mg(OH)_2$ in the $Cu_5(B_{0.02 \text{ M}})Mg_1$ catalyst (Fig. 2a). The characteristic peaks at 42.3°, 50.4°, and 74.1° correspond to the (111), (200) and (220) planes of Cu (PDF#04-0836), respectively. Additionally, four peaks at 29.5°, 36.4°, 42.3° and 61.3° correspond to the (110), (111), (200) and (220) planes of Cu_2O (PDF#05-0667), respectively. Peaks at 35.4°, 39.7°, 48.7°, 53.5° and 66.4° are attributed to the (002), (111), (202), (020) and (310) planes of CuO (PDF#48-1548), respectively. Furthermore, peaks at 18.5°, 32.9°, 58.6° and 68.2° align well with the (001), (100), (110) and (103) planes of $Mg(OH)_2$ (PDF#44-1482), respectively. The XRD pattern demonstrates that the $Cu_5(B_{0.02 \text{ M}})Mg_1$ catalyst mainly comprises Cu, Cu_2O, CuO and $Mg(OH)_2$ crystal phases. On the other hand, XRD patterns of the corresponding reference Cu_5Mg_1, $Cu_5(B_{0.1 \text{ M}})Mg_1$, $Cu(B_{0.02 \text{ M}})$, $Cu_{10}(B_{0.02 \text{ M}})Mg_1$ and $Cu_1(B_{0.02 \text{ M}})Mg_1$ catalysts are provided in Fig. S1.† The $Cu_5(B_{0.1 \text{ M}})Mg_1$, $Cu_{10}(B_{0.02 \text{ M}})Mg_1$ and $Cu_1(B_{0.02 \text{ M}})Mg_1$ catalysts also consist of Cu, Cu_2O, CuO and $Mg(OH)_2$. The $Cu(B_{0.02 \text{ M}})$ catalyst comprises three phases: Cu, Cu_2O and CuO. Notably, for the Cu_5Mg_1 catalyst (lacking the $NaBH_4$ reactant during its preparation), XRD only reveals the existence of CuO (PDF#48-1548), while the $Mg(OH)_2$ (PDF#44-1482) crystalline phases are absent. We propose that this results from the generation of amorphous $Mg(OH)_2$ rather than crystalline $Mg(OH)_2$ when the reducing agent $NaBH_4$ is absent (Fig. S1a†).[34]

Scanning electron microscopy (SEM) and TEM reveal that the as-prepared $Cu_5(B_{0.02 \text{ M}})Mg_1$ catalyst is constructed of nanoclusters (Fig. S2† and Fig. 2b). Energy-dispersive X-ray spectroscopy (EDS) elemental mappings demonstrate a uniform distribution of Cu, Mg, B and O elements on the cata-
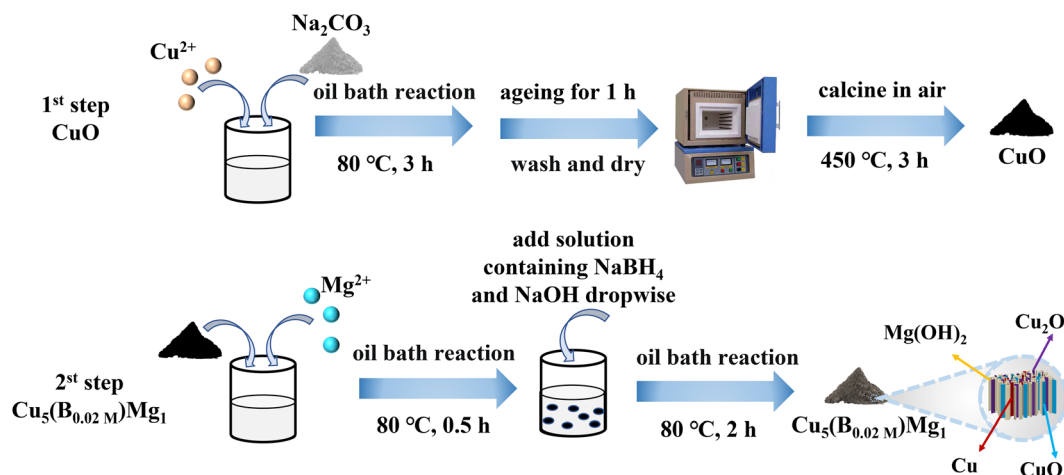
This journal is © the Partner Organisations 2024

Inorg. Chem. Front., 2024, **11**, 4770–4779 | **4771**

Fig. 1 Graphical scheme for the synthesis of the $Cu_5(B_{0.02\ M})Mg_1$ catalyst.

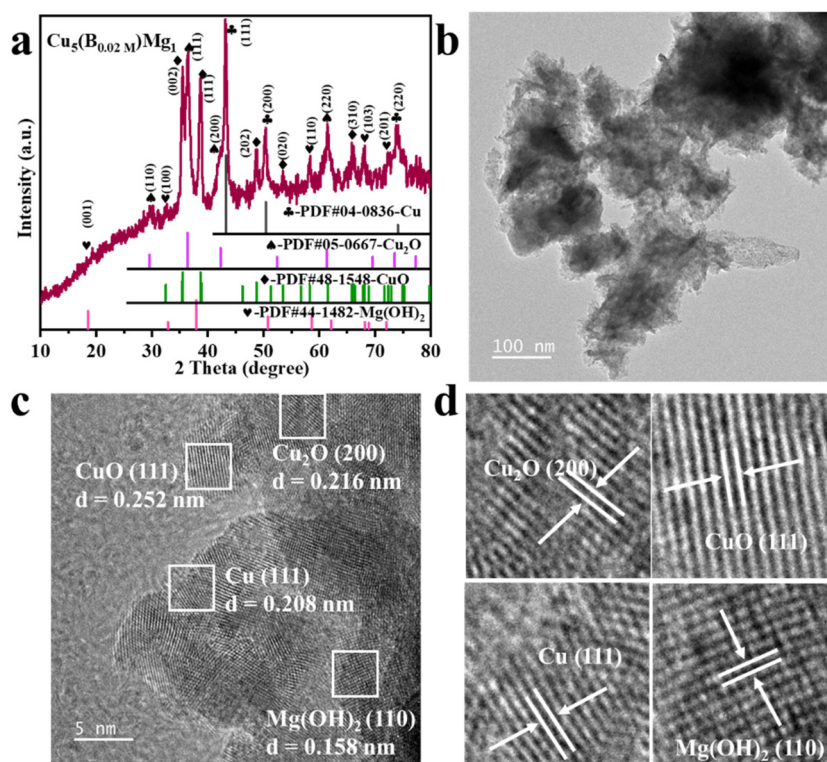**Fig. 2** (a) XRD, (b) TEM and (c) HRTEM characterization of the $Cu_5(B_{0.02\ M})Mg_1$ catalyst. (d) is the enlarged view of (c).

lyst surface (Fig. S2c and d†). SEM and EDS characterization studies were performed on the Cu_5Mg_1, $Cu_5(B_{0.1\ M})Mg_1$, $Cu(B_{0.02\ M})$, $Cu_{10}(B_{0.02\ M})Mg_1$ and $Cu_1(B_{0.02\ M})Mg_1$ catalysts as well, with the corresponding results shown in Fig. S3–S7.† Further HRTEM analysis reveals interplanar spacings of 0.208 (Cu (111)), 0.216 (Cu_2O (200)), 0.252 (CuO (111)) and 0.158 nm ($Mg(OH)_2$ (110)) in the $Cu_5(B_{0.02\ M})Mg_1$ catalyst, consistent with its XRD result (Fig. 2c and d). TEM and HRTEM were also conducted on $Cu(B_{0.02\ M})$ and Cu_5Mg_1 to explore the effect of

Mg and B on the structure of the catalyst (Fig. S8 and S9†). For the $Cu(B_{0.02\ M})$ catalyst, the HRTEM image reveals crystal lattices with interfacial spacings of 0.209, 0.247, and 0.253 nm, coinciding with the Cu (111), Cu_2O (111), and CuO (111) lattices (Fig. S8†). Conversely, the Cu_5Mg_1 catalyst primarily exhibits the CuO (111) crystalline phase, along with some amorphous species (Fig. S9†). Considering TEM and XRD results collectively, we may speculate that the observed amorphous substance in Cu_5Mg_1 arises from some Mg-based amorphous

4772 | *Inorg. Chem. Front.*, 2024, **11**, 4770–4779

This journal is © the Partner Organisations 2024

species formed due to the absence of the $NaBH_4$ reagent (Fig. S9b†).

The electronic structures of the catalysts with different ratios of Cu, Mg and B additions were characterized by XPS (Fig. 3). The Cu 2p XPS spectra demonstrate two peaks corresponding to Cu $2p_{3/2}$ and Cu $2p_{1/2}$ (Fig. 3a and b).[35,36] The peaks at 933.98 and 953.78 eV are attributed to the Cu^{2+} of CuO in Cu_5Mg_1 (Fig. 3a and Table S1†),[37–39] indicating that in the absence of $NaBH_4$ reducing agent, the Cu species in the catalyst mainly exists in the form of Cu^{2+}. Notably, upon $NaBH_4$ addition, the Cu^{2+} bands of $Cu_5(B_{0.02\ M})Mg_1$ and $Cu_5(B_{0.1\ M})Mg_1$ catalysts shift to higher electron binding energies by 0.55 and 0.64 eV, respectively, and at the same time Cu^0/Cu^+ is produced. Additionally, with increasing $NaBH_4$ content, the Cu^0/Cu^+ electron binding energies decrease from 932.43/952.23 eV ($Cu_5(B_{0.02\ M})Mg_1$) to 932.17/951.97 eV ($Cu_5(B_{0.1\ M})Mg_1$) (Fig. 3a and Table S1†).[40–42] These results demonstrate that the $NaBH_4$ content is a key factor affecting the electronic structure of Cu centers. To further differentiate between Cu^0 and Cu^+, Cu LMM Auger electron spectroscopy analysis was performed on $Cu_5(B_{0.02\ M})Mg_1$ and $Cu_5(B_{0.1\ M})Mg_1$ catalysts (Fig. S10†). The two peaks at around 568.00 and 569.75 eV correspond to Cu^0 and Cu^+,[43,44] respectively, confirming the co-existence of Cu^0 and Cu^+ species on these two catalysts. According to previous studies, Cu^0 and Cu^+ played different roles during the CO_2RR. Cu^0 contributed to activating

CO_2 molecules.[45] At the initial stage of the reaction, CO_2 tended to be above the Cu^0 zone. After CO_2 activation, $Cu^{\delta+}$ ($0 < \delta \leq 1$) was proposed to stabilize CO_2 molecules, which can promote the dimerization process between $^*CO$ intermediates and enhance the subsequent C–C coupling.[46,47] In addition, we have investigated the effects of Mg on the valence state of Cu compounds, as provided in Fig. 3b and Table S2.† It can be seen that Mg plays a similar role to B, since with the increasing Mg content, the characteristic XPS band of Cu^{2+} shifts to a higher electron binding energy, while the Cu^0/Cu^+ peak shifts in the opposite direction. These results suggest that the introduced B and Mg elements interact with the surrounding atoms, altering the electron density at the Cu sites. Fig. 3c shows that regardless of the presence of $NaBH_4$, the $Mg(OH)_2$ species persists on the catalysts, as indicated by its characteristic peak at ~1303.60 eV.[48] Taking the XPS and the above XRD/TEM results into comprehensive consideration, it is suggested that the $NaBH_4$ reactant plays a significant role in tuning the crystalline state of the $Mg(OH)_2$ species. In the absence of $NaBH_4$, $Mg(OH)_2$ exists in an amorphous phase, while with $NaBH_4$ addition, $Mg(OH)_2$ exists as crystals. We propose that the existing form of $Mg(OH)_2$ could be a critical influencing factor on the CO_2RR performance of the catalyst. Nonetheless, the high-resolution B 1s spectra of $Cu_5(B_{0.02\ M})Mg_1$ and $Cu_5(B_{0.1\ M})Mg_1$ show two peaks at 191.92 and 191.81 eV, belonging to B–O (Fig. 3d).[49,50] Additionally, the contents

Fig. 3 XPS spectra of Cu 2p in (a) Cu_5Mg_1, $Cu_5(B_{0.02\ M})Mg_1$, $Cu_5(B_{0.1\ M})Mg_1$ (varying the $NaBH_4$ feeding amount while keeping the Cu/Mg ratio at 5 : 1) and (b) $Cu(B_{0.02\ M})$, $Cu_{10}(B_{0.02\ M})Mg_1$, $Cu_5(B_{0.02\ M})Mg_1$ and $Cu_1(B_{0.02\ M})Mg_1$ (varying the ratio of Cu/Mg while keeping the $NaBH_4$ feeding amount the same at 0.02 M). (c) XPS spectra of Mg 1s in Cu_5Mg_1, $Cu_5(B_{0.02\ M})Mg_1$, and $Cu_5(B_{0.1\ M})Mg_1$. (d) The corresponding B 1s XPS spectra of $Cu_5(B_{0.02\ M})Mg_1$ and $Cu_5(B_{0.1\ M})Mg_1$ catalysts.

of Cu, Mg and B elements on the $Cu_5(B_{0.02\ M})Mg_1$ catalyst surface were determined *via* XPS analysis, as provided in Table S3.†

2.2 Electrochemical CO$_2$RR performance in a flow cell

The CO$_2$RR performances of $Cu_5(B_{0.02\ M})Mg_1$, $Cu_5(B_{0.1\ M})Mg_1$, Cu_5Mg_1, $Cu_{10}(B_{0.02\ M})Mg_1$, $Cu_1(B_{0.02\ M})Mg_1$ and $Cu(B_{0.02\ M})$ catalysts were evaluated in 1.0 M KOH electrolyte saturated with CO$_2$ at potentials ranging from -0.77 to -1.97 V. Typical gaseous products (C$_2$H$_4$, CH$_4$, CO, and H$_2$) and liquid products (CH$_3$CH$_2$OH, CH$_3$COOH, CH$_3$OH, and HCOOH) were analyzed (Fig. S11 and S12†). Among these different materials, $Cu_5(B_{0.02\ M})Mg_1$ (Cu : Mg = 5 : 1, NaBH$_4$ = 0.02 M) shows excellent selectivity towards C$_{2+}$ products (Fig. 4 and S13†).

Linear sweep voltammetry (LSV) was first employed to determine the current densities of these Cu catalysts modified by Mg and/or B under CO$_2$RR conditions (Fig. 4a). It is found that the $Cu_5(B_{0.02\ M})Mg_1$ catalyst exhibits a significantly higher current density as compared to the Cu_5Mg_1 and $Cu(B_{0.02\ M})$ catalysts, suggesting a potentially better CO$_2$RR activity. The electrocatalytic products of the three catalysts were then collected during chronoamperometry measurements, and their Faraday efficiencies (FEs) are presented in Fig. 4b–d. Among all the catalysts, $Cu_5(B_{0.02\ M})Mg_1$ shows the highest C$_{2+}$

product selectivity (Fig. 4b). Notably, the FE$_{C_{2+}}$ for the $Cu_5(B_{0.02\ M})Mg_1$ catalyst remains >60% across a wide potential range of 600 mV (from -1.17 to -1.77 V), significantly outperforming Cu_5Mg_1 and $Cu(B_{0.02\ M})$ (Fig. 4b–d). It should be noted that the $Cu_5(B_{0.02\ M})Mg_1$ catalyst also shows a low FE for H$_2$ (FE$_{H_2}$) of <15% within the potential range of -0.77 to -1.57 V, indicating that the hydrogen evolution reaction is effectively inhibited on the catalyst. In particular, a maximal FE$_{C_{2+}}$ of 79.59% at -1.57 V is recorded for $Cu_5(B_{0.02\ M})Mg_1$ (FE$_{C_2H_4}$ = 50.31%, FE$_{C_2H_5OH}$ = 28.58%, with a small amount of CH$_3$COOH), significantly higher than those of Cu_5Mg_1 (FE$_{C_{2+}}$ = 49.53%) and $Cu(B_{0.02\ M})$ catalysts (FE$_{C_{2+}}$ = 31.21%) (Fig. 5a and Table S4†). Furthermore, $Cu_5(B_{0.02\ M})Mg_1$ shows prominently enhanced partial current densities for C$_{2+}$ products ($j_{C_{2+}}$). As depicted in Fig. 5b, $j_{C_{2+}}$ of $Cu_5(B_{0.02\ M})Mg_1$ (-317.03 mA cm^{-2}) is 2.7 and 3.5 times higher than those of Cu_5Mg_1 (-116.74 mA cm^{-2}) and $Cu(B_{0.02\ M})$ (-91.09 mA cm^{-2}) at the same working potential of -1.57 V, suggesting the synergistic promotion of C$_{2+}$ formation on Cu surfaces by Mg and B. In addition, $j_{C_{2+}}$ of $Cu_5(B_{0.02\ M})Mg_1$, Cu_5Mg_1 and $Cu(B_{0.02\ M})$ at more different voltages are shown in Table S5.† Additionally, we have investigated the influence of different ratios of B and Mg during preparation on the electrocatalytic CO$_2$RR activities of the catalysts (Fig. S13†). The results reveal that appropriate amounts of
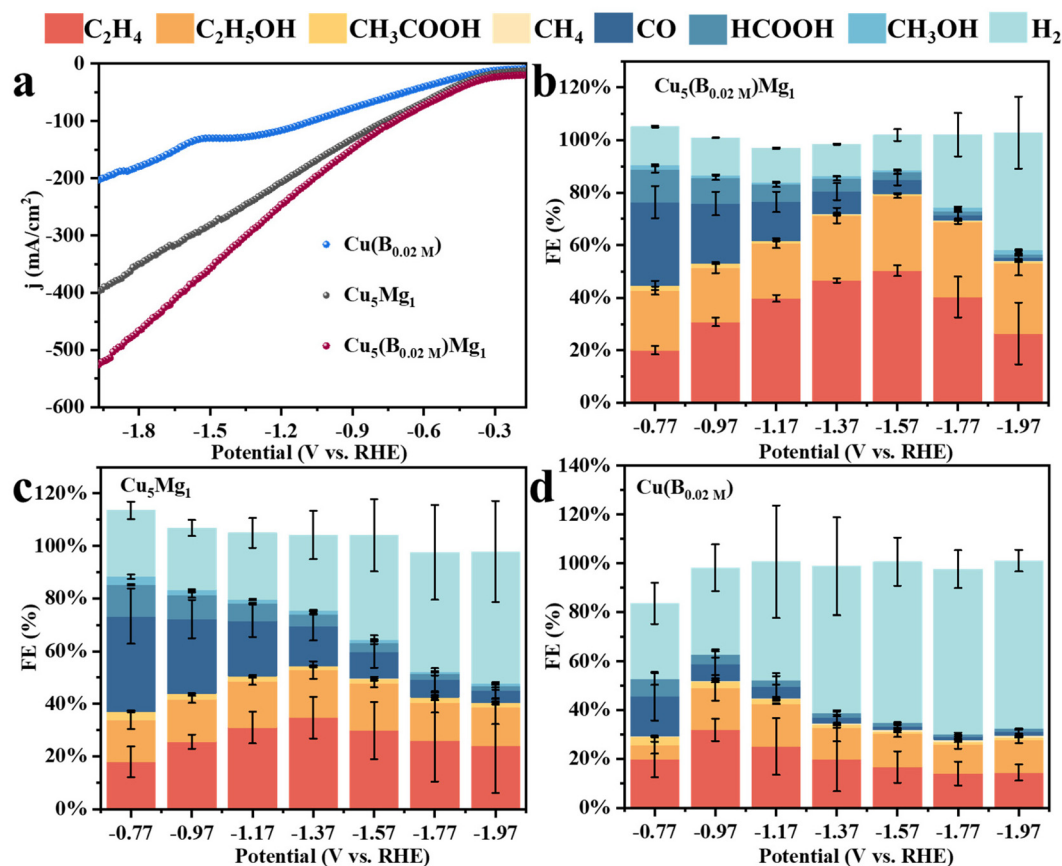
Fig. 4 (a) LSVs of $Cu(B_{0.02\ M})$, Cu_5Mg_1 and $Cu_5(B_{0.02\ M})Mg_1$. The Faraday efficiencies (FEs) of all products for different catalysts: (b) $Cu_5(B_{0.02\ M})Mg_1$, (c) Cu_5Mg_1, and (d) $Cu(B_{0.02\ M})$.

4774 | *Inorg. Chem. Front.*, 2024, **11**, 4770–4779

This journal is © the Partner Organisations 2024

Fig. 5 Electrochemical CO_2RR performance of the $Cu_5(B_{0.02\ M})Mg_1$ catalyst: (a) FEs of C_{2+} (C_2H_4, C_2H_5OH and CH_3COOH) at different potentials and (b) partial current densities of C_{2+}.

$NaBH_4$ and Mg reactants during synthesis are conducive to enhanced C_{2+} selectivity, while excessive usage will reduce C_{2+} products. This could be because the selective promoting and blocking effects of these elements in $Cu_5(B_{0.02\ M})Mg_1$ reach a relatively balanced state for efficient CO_2RR catalysis (Table S4†).[33] Furthermore, we have compared the CO_2RR activities of $Cu_5(B_{0.02\ M})Mg_1$ with other different catalysts in previous literature, which shows that the synergy of Mg and B contributes to a competitive selectivity towards C_{2+} products (Table S6†).

The long-term catalytic performance of $Cu_5(B_{0.02\ M})Mg_1$ for the CO_2RR was measured through chronoamperometry at −1.57 V (Fig. S14†). Within a 10 h period, the current density shows negligible attenuation, but the yield of C_2H_4 gradually decreases over time. After the long-term CO_2RR measurement, $Cu_5(B_{0.02\ M})Mg_1$ was subjected to XRD characterization. The results indicate that the bulk of the catalyst post CO_2RR is primarily composed of Cu (PDF#04-0836), Cu_2O (PDF#05-0667) and $Mg(OH)_2$ (PDF#44-1482), with CuO completely reduced. Notably, the XRD peaks of $Mg(OH)_2$ diminish post CO_2RR, which we believe leads to the decline in the stability of $Cu_5(B_{0.02\ M})Mg_1$ (Fig. S15†). Besides, previous literature studies have suggested that the accumulation of impurities like NO_x, SO_x, and carbon on the catalyst surface can also affect the active sites for the CO_2RR, thereby resulting in a gradual decrease in performance.[51–53] In addition to XRD, XPS characterization was employed to analyze the elemental distribution on the $Cu_5(B_{0.02\ M})Mg_1$ catalyst surface (Fig. S16†). As depicted in Fig. S16a,† copper species, in the form of Cu^0 and Cu^+, predominantly exist on the catalyst surface. The crystalline $Mg(OH)_2$ species nearly vanishes after the long-term CO_2RR, therefore contributing to the decline in the performance of the $Cu_5(B_{0.02\ M})Mg_1$ catalyst (Fig. S16b†). Additionally, XPS results show that the B element still exists on the catalyst (Fig. S16c†).

To study the enhanced CO_2RR performance of the $Cu_5(B_{0.02\ M})Mg_1$ catalyst, the electrochemically active surface areas of all the electrocatalysts were estimated by calculating their double layer capacitances (C_{dl}) (Fig. S17 and S18†). Obviously, compared with Cu_5Mg_1 (2.83 mF cm^{-2}), $Cu_5(B_{0.1\ M})$

Mg_1 (1.61 mF cm^{-2}), $Cu(B_{0.02\ M})$ (0.99 mF cm^{-2}), $Cu_{10}(B_{0.02\ M})$ Mg_1 (2.20 mF cm^{-2}) and $Cu_1(B_{0.02\ M})Mg_1$ (1.19 mF cm^{-2}), $Cu_5(B_{0.02\ M})Mg_1$ (3.28 mF cm^{-2}) has the largest C_{dl} value, revealing that the $Cu_5(B_{0.02\ M})Mg_1$ catalyst can provide more active sites for the CO_2RR. Meanwhile, it is worth noting that the active surface area of Cu_5Mg_1 is lower than that of $Cu_5(B_{0.02\ M})$ Mg_1, which may be due to the formation of amorphous Mg $(OH)_2$ on the catalyst surface, causing part of the active sites to be covered due to the "stacking" effect, thus reducing the overall catalytic activity of Cu_5Mg_1.[54] Electrochemical impedance spectroscopy measurements have also been performed to investigate the charge transfer properties of the catalysts (Fig. S19†). It is obvious that an appropriate co-modification of Mg and B could accelerate the charge transfer process during the CO_2RR.

In situ Raman spectroscopy was further conducted to examine the effects of B and/or Mg on the valence of Cu (Cu^0, Cu^+ or Cu^{2+}) as well as to probe probable intermediates during the CO_2RR (Fig. 6). Fig. 6a presents the *in situ* Raman spectra of the $Cu_5(B_{0.02\ M})Mg_1$ catalyst in 1.0 M KOH electrolyte (saturated with CO_2) during the CO_2RR. At the open circuit voltage, three characteristic peaks are observed at around 147, 522 and 626 cm^{-1}, attributed to Cu_2O.[55–57] After applying a cathodic potential of −0.37 V, a new Raman band appears at 703 cm^{-1} on the $Cu_5(B_{0.02\ M})Mg_1$ catalyst, corresponding to surface δCO_2^-, which represents the umbrella motion of oxygen atoms of the $*CO^{2-}$ intermediate. Previous studies recognized $*CO_2^-$ as the initial intermediate just after CO_2 activation.[58] At the same time, Raman peaks at 290 and 374 cm^{-1} are recorded, assigned to the frustrated rotation and tensile vibrations of Cu-CO, respectively.[59–61] Besides, the band at 1071 cm^{-1} corresponds to the symmetric C–O stretching band of CO_3^{2-} from the electrolyte.[62,63] It is worth noting that over the wide potential range of −0.37 to −1.37 V, Cu_2O peaks at 147, 522 and 626 cm^{-1} consistently appear on the $Cu_5(B_{0.02\ M})Mg_1$ catalyst, indicating that the CuO species on the catalyst surface has been completely reduced, while Cu^+ persists, probably being the reactive sites during the electrochemical CO_2RR. We propose that the robust stability of Cu_2O species over a wide potential window is attributed to the synergy of B and crystal-

This journal is © the Partner Organisations 2024

Inorg. Chem. Front., 2024, **11**, 4770–4779 | **4775**

Fig. 6 The *in situ* Raman spectra of (a) $Cu_5(B_{0.02\ M})Mg_1$, (b) Cu_5Mg_1 and (c) $Cu(B_{0.02\ M})$ catalysts at various potentials in 1.0 M KOH electrolyte during CO_2RR catalysis.

line $Mg(OH)_2$. According to previous literature, the Cu^+ on the catalyst surface is crucial for the formation of multi-carbon products.[64–67] The Raman spectra over −1.37 V cannot be collected because of the accumulation of gaseous products on the catalyst surface that block signals. Nevertheless, Raman signals for Cu_5Mg_1 and $Cu(B_{0.02\ M})$ are also recorded under the same conditions as $Cu_5(B_{0.02\ M})Mg_1$ to explore the influences of Mg and B on the Cu catalysts, as shown in Fig. 6b and c. In contrast to the $Cu_5(B_{0.02\ M})Mg_1$ catalyst, Cu_2O peaks vanish at only −0.87 V and −0.97 V for Cu_5Mg_1 and $Cu(B_{0.02\ M})$ catalysts, respectively. In addition, unlike the $Cu_5(B_{0.02\ M})Mg_1$ catalyst which displays characteristic bands of *CO and $*CO_2^-$ at −0.37 V, neither Cu_5Mg_1 nor the $Cu(B_{0.02\ M})$ catalyst shows these bands until −0.47 V. Hence, it is evident that compared to the Cu_5Mg_1 and $Cu(B_{0.02\ M})$ catalysts, the collaborative effect of Mg and B, which induces the formation of crystalline $Mg(OH)_2$ species in the catalyst structure, facilitates the early formation of $*CO_2^-$ and *CO intermediates during the CO_2RR.

A previous study by Yang *et al.* utilized cerium as a self-sacrificing agent to stabilize Cu^+ in their catalyst, taking advantage of the easy redox properties of Ce^{3+}/Ce^{4+}. Their *in situ* Raman and Fourier transform infrared spectroscopy results demonstrated that the stabilized Cu^+ components promoted C–C coupling under the CO_2RR. DFT calculations further revealed that strong *CO adsorption and low C–C coupling energy were conducive to the formation of C_2H_5OH.[61] Wang *et al.* prepared an ultra-thin 2D Cu_2O nanosheet (Cu_2O-NS) catalyst with abundant oxygen vacancies. *In situ* Raman spectroscopy and DFT calculations supported that Cu_2O-NS prevented the reduction of surface Cu oxides, thereby stabilizing Cu^+ and enhancing the conversion of CO_2 to C_{2+}.[68] Similarly, in our work, Cu^+ stabilization is achieved through the introduction of appropriate Mg and B into Cu materials. We found that the addition of the $NaBH_4$ reactant can tune the amorphous or crystalline phases of $Mg(OH)_2$. Crystallized $Mg(OH)_2$ is crucial for prolonging the lifetime of Cu^+ during the CO_2RR and facilitating the activation of CO_2 on the Cu surface to

generate key *CO intermediates for C–C coupling. Consequently, this enhances the selectivity towards C_{2+} products of our catalyst.

3 Conclusion

Overall, a simple two-step method involving calcination and subsequent wet chemical reduction is developed to construct a Cu-based electrocatalyst modified by crystalline $Mg(OH)_2$ and B. XRD, TEM, and XPS analyses indicate that the addition of the $NaBH_4$ reactant can induce the formation of crystalline $Mg(OH)_2$, which is proposed to enhance the conversion of CO_2 to C_{2+} during the CO_2RR compared to amorphous $Mg(OH)_2$. In support of this, *in situ* Raman spectroscopy reveals that the synergy of crystalline $Mg(OH)_2$ and B can stabilize Cu^+ at rather cathodic potentials during the CO_2RR process, effectively producing and preserving the *CO intermediates, therefore greatly enhancing the *CO–CO coupling. As a result, the $FE_{C_{2+}}$ surpasses 60% on the $Cu_5(B_{0.02\ M})Mg_1$ electrocatalyst over a wide potential window of 600 mV (−1.17 to −1.77 V). In particular, at −1.57 V, the catalyst exhibits a $FE_{C_{2+}}$ as high as 79.59%, demonstrating enormous potential for its scalable applications. This work not only provides a low-cost, simple and effective synthesis method for efficient electrocatalysts but also offers an in-depth understanding of the active sites and reaction intermediates during CO_2-to-C_{2+} conversion. We believe that this will help inspire the rational design of future CO_2RR electrocatalysts.

Conflicts of interest

The authors declare that they have no known competing financial interests or personal relationships that could have appeared to influence the work reported in this paper.

4776 | *Inorg. Chem. Front.*, 2024, **11**, 4770–4779

This journal is © the Partner Organisations 2024

Acknowledgements

References

1 H. H. Wang, N. Wen, Y. Q. Wang, X. L. Jiao, Y. G. Xia and D. R. Chen, Boosting Electrochemical Reduction of CO_2 to Formate over Oxygen Vacancy Stabilized Copper–Tin Dual Single Atoms Catalysts, *Adv. Funct. Mater.*, 2023, **33**, 2303473.

2 J. Y. Liu, P. S. Li, J. H. Bi, S. Q. Jia, Y. Wang, X. C. Kang, X. F. Sun, Q. G. Zhu and B. X. Han, Switching between C_{2+} Products and CH_4 in CO_2 Electrolysis by Tuning the Composition and Structure of Rare-Earth/Copper Catalysts, *J. Am. Chem. Soc.*, 2023, **145**, 23037–23047.

3 J. Yin, J. Jin, Z. Y. Yin, L. Zhu, X. Du, Y. Peng, P. Xi, C. H. Yan and S. H. Sun, The built-in electric field across FeN/Fe_3N interface for efficient electrochemical reduction of CO_2 to CO, *Nat. Commun.*, 2023, **14**, 1724.

4 P. S. Li, J. H. Bi, J. Y. Liu, Y. Wang, X. C. Kang, X. F. Sun, J. L. Zhang, Z. M. Liu, Q. G. Zhu and B. X. Han, p–d Orbital Hybridization Induced by p-Block Metal-Doped Cu Promotes the Formation of C_{2+} Products in Ampere-Level CO_2 Electroreduction, *J. Am. Chem. Soc.*, 2023, **145**, 4675–4682.

5 Z. Y. Zhang, H. Tian, L. Bian, S. Z. Liu, Y. Liu and Z. L. Wang, Cu-Zn-based alloy/oxide interfaces for enhanced electroreduction of CO_2 to C_{2+} products, *J. Energy Chem.*, 2023, **83**, 90–97.

6 R. Shi, J. Guo, X. Zhang, G. I. N. Waterhouse, Z. Han, Y. Zhao, L. Shang, C. Zhou, L. Jiang and T. Zhang, Efficient wettability-controlled electroreduction of CO_2 to CO at Au/C interfaces, *Nat. Commun.*, 2020, **11**, 3028.

7 X. T. Wang, Z. Z. Wang, Y. Li, J. T. Wang and G. K. Zhang, Efficient photocatalytic CO_2 conversion over 2D/2D Ni-doped $CsPbBr_3/Bi_3O_4Br$ Z-scheme heterojunction: Critical role of Ni doping, boosted charge separation and mechanism study, *Appl. Catal., B*, 2022, **319**, 121895.

8 J. Wu, Y. Huang, W. Ye and Y. Li, CO_2 Reduction: From the Electrochemical to Photochemical Approach, *Adv. Sci.*, 2017, **4**, 1700194.

9 Z. Li, R. Wu, L. Zhao, P. Li, X. Wei, J. Wang, J. S. Chen and T. Zhang, Metal-support interactions in designing noble metal-based catalysts for electrochemical CO_2 reduction: Recent advances and future perspectives, *Nano Res.*, 2021, **14**, 3795–3809.

10 Y. Yang, S. Louisia, S. M. Yu, J. B. Jin, I. Roh, C. B. Chen, M. V. F. Guzman, J. Feijóo, P. C. Chen, H. S. Wang, C. J. Pollock, X. Huang, Y. T. Shao, C. Wang, D. A. Muller, H. D. Abruña and P. D. Yang, Operando studies reveal active Cu nanograins for CO_2 electroreduction, *Nature*, 2023, **614**, 262–269.

11 S. Y. Lee, J. M. Kim, G. Bak, E. C. Lee, D. Kim, S. Yoo, J. Kim, H. Yun and Y. J. Hwang, Probing Cation Effects on *CO Intermediates from Electroreduction of CO_2 through Operando Raman Spectroscopy, *J. Am. Chem. Soc.*, 2023, **145**, 23068–23075.

12 T. Ahmad, S. Liu, M. Sajid, K. Li, M. Ali, L. Liu and W. Chen, Electrochemical CO_2 reduction to C_{2+} products using Cu-based electrocatalysts: A review, *Nano Res. Energy*, 2022, **1**, e9120021.

13 C. Liu, M. M. Wang, J. Y. Ye, L. B. Liu, L. G. Li, Y. H. Li and X. Q. Huang, Highly Selective CO_2 Electroreduction to C_{2+} Products over Cu_2O-Decorated 2D Metal–Organic Frameworks with Rich Heterogeneous Interfaces, *Nano Lett.*, 2023, **23**, 1474–1480.

14 P. De Luna, R. Quintero-Bermudez, C. T. Dinh, M. B. Ross, O. S. Bushuyev, P. Todorović, T. Regier, S. O. Kelley, P. D. Yang and E. H. Sargent, Catalyst electro-redeposition controls morphology and oxidation state for selective carbon dioxide reduction, *Nat. Catal.*, 2018, **1**, 103–110.

15 L. C. Ding, N. N. Zhu, Y. Hu, Z. Chen, P. Song, T. Sheng, Z. C. Wu and Y. J. Xiong, Over 70% Faradaic Efficiency for CO_2 Electroreduction to Ethanol Enabled by Potassium Dopant–Tuned Interaction between Copper Sites and Intermediates, *Angew. Chem., Int. Ed.*, 2022, **61**, e202209268.

16 C. Peng, G. Luo, J. B. Zhang, M. H. Chen, Z. Q. Wang, T. K. Sham, L. J. Zhang, Y. F. Li and G. F. Zheng, Double sulfur vacancies by lithium tuning enhance CO_2 electroreduction to n-propanol, *Nat. Catal.*, 2021, **12**, 1580.

17 Y. R. Lin, D. U. Lee, S. Q. Tan, D. M. Koshy, T. Y. Lin, L. Wang, D. Corral, J. E. Avilés Acosta, J. A. Z. Zeledon, V. A. Beck, S. E. Baker, E. B. Duoss, C. Hahn and T. F. Jaramillo, Vapor–Fed Electrolyzers for Carbon Dioxide Reduction Using Tandem Electrocatalysts: Cuprous Oxide Coupled with Nickel–Coordinated Nitrogen–Doped Carbon, *Adv. Funct. Mater.*, 2022, **32**, 2113252.

18 X. P. Qin, S. Q. Zhu, F. Xiao, L. L. Zhang and M. H. Shao, Active Sites on Heterogeneous Single-Iron-Atom Electrocatalysts in CO_2 Reduction Reaction, *ACS Energy Lett.*, 2019, **4**, 1778–1783.

19 Y. J. Shi, Y. J. Wang, J. Y. Yu, Y. K. Chen, C. Q. Fang, D. Jiang, Q. H. Zhang, L. Gu, X. W. Yu, X. Li, H. Liu and W. J. Zhou, Superscalar Phase Boundaries Derived Multiple Active Sites in $SnO_2/Cu_6Sn_5/CuO$ for Tandem Electroreduction of CO_2 to Formic Acid, *Adv. Energy Mater.*, 2023, **13**, 2203506.

20 P. T. Wang, M. Qiao, Q. Shao, Y. C. Pi, X. Zhu, Y. F. Li and X. Q. Huang, Phase and structure engineering of copper tin heterostructures for efficient electrochemical carbon dioxide reduction, *Nat. Catal.*, 2018, **9**, 4933.

21 D. G. Park, J. W. Choi, H. J. Chun, H. S. Jang, H. B. Lee, W. H. Choi, B. C. Moon, K. H. Kim, M. G. Kim, K. M. Choi, B. C. Han and J. K. Kang, Increasing CO Binding Energy and Defects by Preserving Cu Oxidation State via O_2-Plasma-Assisted N Doping on CuO Enables High C_{2+}

This journal is © the Partner Organisations 2024

Inorg. Chem. Front., 2024, **11**, 4770–4779 | **4777**

Selectivity and Long-Term Stability in Electrochemical CO_2 Reduction, *ACS Catal.*, 2023, **13**, 9222–9233.

22 G. Park, H. Kim, G. H. Han, J. Ha, J. Y. Seo, M. J. Kang, M. G. Seo, Y. H. Choi, S. Y. Kim and S. H. Ahn, The effect of Cu oxidation states on C_2H_4 production from electrochemical CO_2 conversion, *J. CO$_2$ Util.*, 2023, **75**, 102569.

23 R. B. Sun, C. Wei, Z. X. Huang, S. W. Niu, X. Han, C. Chen, H. R. Wang, J. Song, J. D. Yi, G. Wu, D. W. Rao, X. S. Zheng, Y. Wu, G. M. Wang and X. Hong, $Cu_{2+1}O/CuO_x$ heterostructures promote the electrosynthesis of C_{2+} products from CO_2, *Nano Res.*, 2022, **16**, 4698–4705.

24 H. H. Yang, S. Y. Li and Q. Xu, Efficient strategies for promoting the electrochemical reduction of CO_2 to C_{2+} products over Cu-based catalysts, *Chin. J. Catal.*, 2023, **48**, 32–65.

25 J. Wang, J. J. Liu, Y. Q. Song, S. B. Geng, Z. H. Peng, J. L. Yu, F. Liu, Y. H. Wang, S. B. Xi, Z. J. Zhang and Z. X. Fan, Simultaneous Defect and Size Control of Metal–Organic Framework Nanostructures for Highly Efficient Carbon Dioxide Electroreduction to Multicarbon Products, *ACS Mater. Lett.*, 2023, **5**, 2121–2130.

26 J. W. Su, D. H. Pan, Y. Dong, Y. Y. Zhang, Y. L. Tang, J. Sun, L. J. Zhang, Z. Q. Tian and L. Chen, Ultrafine Fe_2C Iron Carbide Nanoclusters Trapped in Topological Carbon Defects for Efficient Electroreduction of Carbon Dioxide, *Adv. Energy Mater.*, 2023, **13**, 2204391.

27 R. G. Cai, M. Z. Sun, F. Yang, M. Ju, Y. P. Chen, M. D. Gu, B. L. Huang and S. H. Yang, Engineering Cu(I)/Cu(0) interfaces for efficient ethanol production from CO_2 electroreduction, *Chem*, 2023, **10**, 1–23.

28 Y. P. Zang, T. F. Liu, P. F. Wei, H. F. Li, Q. Wang, G. X. Wang and X. H. Bao, Selective CO_2 Electroreduction to Ethanol over a Carbon–Coated CuO_x Catalyst, *Angew. Chem., Int. Ed.*, 2022, **61**, e202209629.

29 C. F. Wen, M. Zhou, P. F. Liu, Y. W. Liu, X. F. Wu, F. X. Mao, S. Dai, B. B. Xu, X. L. Wang, Z. Jiang, P. Hu, S. Yang, H. F. Wang and H. G. Yang, Highly Ethylene–Selective Electrocatalytic CO_2 Reduction Enabled by Isolated Cu–S Motifs in Metal–Organic Framework Based Precatalysts, *Angew. Chem., Int. Ed.*, 2021, **61**, e202111700.

30 Y. Yao, Y. Zhou, X. Liu, Y. Li, D. Wang, X. Chi, X. Wang, R. Zhao, H. Zhang, Y. Sun, Z.-Y. Yang, Y. Wei and Y.-M. Yan, Restraining lattice oxygen of Cu_2O by enhanced Cu–O hybridization for selective and stable production of ethylene with CO_2 electroreduction, *J. Mater. Chem. A*, 2022, **10**, 20914–20923.

31 S. Sinha and J. J. Jiang, Main group elements in electrochemical hydrogen evolution and carbon dioxide reduction, *Chem. Commun.*, 2023, **59**, 11767–11779.

32 C. Peng, J. Ma, G. Luo, S. Yan, J. Zhang, Y. Chen, N. Chen, Z. Wang, W. Wei, T. K. Sham, Y. Zheng, M. Kuang and G. Zheng, (111) Facet-oriented Cu_2Mg Intermetallic Compound with Cu_3-Mg Sites for CO_2 Electroreduction to Ethanol with Industrial Current Density, *Angew. Chem., Int. Ed. Engl.*, 2024, e202316907.

33 M. C. Xie, Y. Shen, W. C. Ma, D. Y. Wei, B. Zhang, Z. H. Wang, Y. H. Wang, Q. H. Zhang, S. J. Xie, C. Wang and Y. Wang, Fast Screening for Copper–Based Bimetallic Electrocatalysts: Efficient Electrocatalytic Reduction of CO_2 to C_{2+} Products on Magnesium–Modified Copper, *Angew. Chem., Int. Ed.*, 2022, **61**, e202213423.

34 J. Fan, X. Zhang, M. Han, X. Xiang, C. Guo, Y. Lin, N. Shi, D. Xu, Y. Lai and J. Bao, Amorphous Ni–Fe–Mo Oxides Coupled with Crystalline Metallic Domains for Enhanced Electrocatalytic Oxygen Evolution by Promoted Lattice–Oxygen Participation, *Small*, 2023, **20**, 2303927.

35 Y. Z. Li, Z. B. Wang, C. Li, F. Qi, P. W. Yan, Y. P. Wang, M. F. He, Z. L. Chen, Q. Wang, Y. Wang, H. Zheng, A. Ikhlaq, J. Kumirska, E. Maria Siedlecka and O. Ismailova, Reducing agents enhanced prometon degradation by $CuBi_2O_4$/peroxymonosulfate: Development of interfacial electron transport and circulation of Cu^+/Cu^{2+}, *Chem. Eng. J.*, 2023, **470**, 144387.

36 Z. P. Ma, T. Wan, D. Zhang, J. A. Yuwono, C. Tsounis, J. Jiang, Y. H. Chou, X. Y. Lu, P. V. Kumar, Y. H. Ng, D. Chu, C. Y. Toe, Z. J. Han and R. Amal, Atomically Dispersed Cu Catalysts on Sulfide-Derived Defective Ag Nanowires for Electrochemical CO_2 Reduction, *ACS Nano*, 2023, **17**, 2387–2398.

37 Z. Q. Zhang, J. L. Liang, W. Zhang, M. Zhou, X. L. Zhu, Z. Y. Liu, Y. Li, Z. Q. Guan, C. S. Lee, P. K. Wong, H. M. Li and Z. F. Jiang, Modified-pollen confined hybrid system: A promising union for visible-light-driven photocatalytic antibiotic degradation, *Appl. Catal., B*, 2023, **330**, 122621.

38 X. L. Zhou, J. Q. Shan, L. Chen, B. Y. Xia, T. Ling, J. J. Duan, Y. Jiao, Y. Zheng and S. Z. Qiao, Stabilizing Cu^{2+} Ions by Solid Solutions to Promote CO_2 Electroreduction to Methane, *J. Am. Chem. Soc.*, 2022, **144**, 2079–2084.

39 D. X. Tan, J. L. Zhang, L. Yao, X. N. Tan, X. Y. Cheng, Q. Wan, B. X. Han, L. R. Zheng and J. Zhang, Multi-shelled CuO microboxes for carbon dioxide reduction to ethylene, *Nano Res.*, 2020, **13**, 768–774.

40 V. Okatenko, A. Loiudice, M. A. Newton, D. C. Stoian, A. Blokhina, A. N. Chen, K. Rossi and R. Buonsanti, Alloying as a Strategy to Boost the Stability of Copper Nanocatalysts during the Electrochemical CO_2 Reduction Reaction, *J. Am. Chem. Soc.*, 2023, **145**, 5370–5383.

41 P. T. Wang, H. Yang, C. Tang, Y. Wu, Y. Zheng, T. Cheng, K. Davey, X. Q. Huang and S. Z. Qiao, Boosting electrocatalytic CO_2−to−ethanol production via asymmetric C–C coupling, *Nat. Catal.*, 2022, **13**, 3754.

42 W. Lai, L. H. Ge, H. Yang, Y. L. Deng, H. M. Li, B. Ouyang, L. Xu and J. Bao, Reprogramming the redox states of nickel via interface engineering and heteroatom doping to boost overall water splitting, *J. Mater. Chem. A*, 2022, **10**, 10525–10539.

43 J. H. Jang, S. Q. Zhu, E. P. Delmo, T. H. Li, Q. L. Zhao, Y. N. Wang, L. L. Zhang, H. W. Huang, J. J. Ge and M. H. Shao, Facile design of oxide–derived Cu nanosheet electrocatalyst for CO_2 reduction reaction, *EcoMat*, 2023, **5**, e12334.

44 Y. Zhang, Z. B. Si, H. H. Du, Y. L. Deng, Q. K. Zhang, Z. L. Wang, Q. Yu and H. Xu, Selective CO_2 Reduction to

4778 | *Inorg. Chem. Front.*, 2024, **11**, 4770–4779

This journal is © the Partner Organisations 2024

Ethylene Over a Wide Potential Window by Copper Nanowires with High Density of Defects, *Inorg. Chem.*, 2022, **61**, 20666–20673.

45 X.-J. Cui, Y.-Q. Qiu, H.-Q. Wang and C.-G. Liu, Direct coupling of two inert CO_2 molecules to form a C–C bond on the Cu^0 atomic interfaces of the nitrogen-doped graphene-supported Cu_4 cluster, *Inorg. Chem. Front.*, 2024, **11**, 85–97.

46 G. M. Tomboc, S. Choi, T. Kwon, Y. J. Hwang and K. Lee, Potential Link between Cu Surface and Selective CO_2 Electroreduction: Perspective on Future Electrocatalyst Designs, *Adv. Mater.*, 2020, **32**, e1908398.

47 Z. Li, Z. Liu, S. Li, Y. Pei, D. Li, J. Mao, R. Zhou, C. Qiu, Y. Lu and B. Zhang, Modulating the localized electronic distribution of Cu species during reconstruction for enhanced electrochemical CO_2 reduction to C_{2+} products, *J. Mater. Chem. A*, 2024, DOI: **10.1039/d4ta01184h**.

48 S. J. Han, L. L. Mao, T. Wu and H. Z. Wang, Homogeneous polyethersulfone hybrid membranes prepared with in-suit synthesized magnesium hydroxide nanoparticles by phase inversion method, *J. Membr. Sci.*, 2016, **516**, 47–55.

49 H. Zhang, D. Y. Zhang, M. Y. Guo, Z. Huang, X. Wang, C. Q. Gao, F. Gao, M. Terrones and Y. Q. Wang, Combustion Activation Induced Solid–State Synthesis for N, B Co–Doped Carbon/Zinc Borate Anode with a Boosting of Sodium Storage Performance, *Adv. Sci.*, 2023, **10**, 2207751.

50 H. Q. Peng, X. Ming, K. Pang, Y. R. Chen, J. Zhou, Z. Xu, Y. J. Liu and C. Gao, Highly electrically conductive graphene papers via catalytic graphitization, *Nano Res.*, 2022, **15**, 4902–4908.

51 J. Leverett, J. A. Yuwono, P. Kumar, T. Tran-Phu, J. Qu, J. Cairney, X. Wang, A. N. Simonov, R. K. Hocking, B. Johannessen, L. Dai, R. Daiyan and R. Amal, Impurity Tolerance of Unsaturated Ni-N-C Active Sites for Practical Electrochemical CO_2 Reduction, *ACS Energy Lett.*, 2022, **7**, 920–928.

52 S. Van Daele, L. Hintjens, S. Hoekx, B. Bohlen, S. Neukermans, N. Daems, J. Hereijgers and T. Breugelmans, How flue gas impurities affect the electrochemical reduction of CO_2 to CO and formate, *Appl. Catal., B*, 2024, **341**, 123345.

53 W. Lai, Y. Qiao, Y. Wang and H. Huang, Stability Issues in Electrochemical CO_2 Reduction: Recent Advances in Fundamental Understanding and Design Strategies, *Adv. Mater.*, 2023, **35**, e2306288.

54 G. X. Zhang, X. L. Zheng, X. M. Cui, J. Wang, J. H. Liu, J. F. Chen and Q. Xu, Doping of Vanadium into Bismuth Oxide Nanoparticles for Electrocatalytic CO_2 Reduction, *ACS Appl. Nano Mater.*, 2022, **5**, 15465–15472.

55 D. Ren, Y. L. Deng, A. D. Handoko, C. S. Chen, S. Malkhandi and B. S. Yeo, Selective Electrochemical Reduction of Carbon Dioxide to Ethylene and Ethanol on Copper(I) Oxide Catalysts, *ACS Catal.*, 2015, **5**, 2814–2821.

56 S. J. Mu, H. L. Lu, Q. B. Wu, L. Li, R. I. Zhao, C. Long and C. H. Cui, Hydroxyl radicals dominate reoxidation of oxide-derived Cu in electrochemical CO_2 reduction, *Nat. Commun.*, 2022, **13**, 3694.

57 H. T. Du, L. X. Liu, P. Li, Q. H. Min, S. J. Guo and W. L. Zhu, Enriching Reaction Intermediates in Multishell Structured Copper Catalysts for Boosted Propanol Electrosynthesis from Carbon Monoxide, *ACS Nano*, 2023, **17**, 8663–8670.

58 Y. Zhao, X. G. Zhang, N. Bodappa, W. M. Yang, Q. Liang, P. M. Radjenovica, Y. H. Wang, Y. J. Zhang, J. C. Dong, Z. Q. Tian and J. F. Li, Elucidating electrochemical CO_2 reduction reaction processes on Cu(*hkl*) single-crystal surfaces by in situ Raman spectroscopy, *Energy Environ. Sci.*, 2022, **15**, 3968–3977.

59 Y. L. Deng, Y. Huang, D. Ren, A. D. Handoko, Z. W. Seh, P. Hirunsit and B. S. Yeo, On the Role of Sulfur for the Selective Electrochemical Reduction of CO_2 to Formate on CuS_x Catalysts, *ACS Appl. Mater. Interfaces*, 2018, **10**, 28572–28581.

60 D. Ren, J. H. Fong and B. S. Yeo, The effects of currents and potentials on the selectivities of copper toward carbon dioxide electroreduction, *Nat. Commun.*, 2018, **9**, 925.

61 Z. Yang, D. G. Ji, Z. Li, Z. D. He, Y. Hu, J. Yin, Y. H. Hou, P. X. Xi and C. H. Yan, Ceo_2/Cus Nanoplates Electroreduce Co_2 to Ethanol with Stabilized Cu^+ Species, *Small*, 2023, **19**, 2303099.

62 X. P. Yan, M. L. Zhang, Y. Z. Chen, Y. H. Wu, R. Z. Wu, Q. Wan, C. X. Liu, T. T. Zheng, R. J. Feng, J. Zhang, C. J. Chen, C. Xia, Q. G. Zhu, X. F. Sun, Q. L. Qian and B. X. Han, Synergy of Cu/C_3N_4 Interface and Cu Nanoparticles Dual Catalytic Regions in Electrolysis of CO to Acetic Acid, *Angew. Chem., Int. Ed.*, 2023, **62**, e202301507.

63 R. Amirbeigiarab, J. Tian, A. Herzog, C. R. Qiu, A. Bergmann, B. R. Cuenya and O. M. Magnussen, Atomic-scale surface restructuring of copper electrodes under CO_2 electroreduction conditions, *Nat. Catal.*, 2023, **6**, 837–846.

64 H. Zhang, Y. Qiao, Y. Wang, Y. Zheng and H. Huang, In situ oxidative etching-enabled synthesis of hollow Cu_2O nanocrystals for efficient CO_2RR into C_{2+} products, *Sustainable Energy Fuels*, 2022, **6**, 4860–4865.

65 M. Fang, M. Wang, Z. Wang, Z. Zhang, H. Zhou, L. Dai, Y. Zhu and L. Jiang, Hydrophobic, Ultrastable $Cu^{\delta+}$ for Robust CO_2 Electroreduction to C_2 Products at Ampere-Current Levels, *J. Am. Chem. Soc.*, 2023, **145**, 11323–11332.

66 Y. Zhou, Y. Yao, R. Zhao, X. Wang, Z. Fu, D. Wang, H. Wang, L. Zhao, W. Ni, Z. Yang and Y. M. Yan, Stabilization of Cu^+ via Strong Electronic Interaction for Selective and Stable CO_2 Electroreduction, *Angew. Chem., Int. Ed.*, 2022, **61**, e202205832.

67 H. Cheng, S. Jia, J. Jiao, X. Chen, T. Deng, C. Xue, M. Dong, J. Zeng, C. Chen, H. Wu, M. He and B. Han, Stabilization of Cu^+ sites by amorphous Al_2O_3 to enhance electrochemical CO_2 reduction to C_{2+} products, *Green Chem.*, 2024, **26**, 2599–2604.

68 P. Wang, S. Meng, B. Zhang, M. He, P. Li, C. Yang, G. Li and Z. Li, Sub-1 nm Cu_2O Nanosheets for the Electrochemical CO_2 Reduction and Valence State-Activity Relationship, *J. Am. Chem. Soc.*, 2023, **145**, 26133–26143.

This journal is © the Partner Organisations 2024

Inorg. Chem. Front., 2024, **11**, 4770–4779 | **4779**